The Influence of Salt Erosion on the Mechanical Performances of Ultra-High-Performance Concrete with Secondary Aluminum Dross

Houchao Sun [1], Weixiang Sun [2], Feiting Shi [1], Lu Miao [2] and Hui Wang [1,3,*]

1   School of Civil Engineering, Yancheng Institute of Technology, Yancheng 224051, China
2   China Construction Infrastructure Co., Ltd., Beijing 100020, China
3   School of Civil Engineering and Geographic Environment, Ningbo University, Ningbo 315000, China
*   Correspondence: huiwang123@aliyun.com

Abstract: Secondary aluminum dross containing a large amount of active substance can be used to prepare concrete. The mechanical strengths, the mass loss rate (MR) and the relative dynamic modulus of elasticity (RME) of ultra-high-performance concrete with secondary aluminum dross are researched. The NaCl freeze–thaw cycles (F-Cs) and dry–wet alternation (D-A) effects with NaCl and Na_2SO_4 are considered. The corresponding permeability of chloride ions and the carbonation depth (D_c) are obtained. The scanning electron microscope (SEM) photos are researched to reveal the variation of the mechanical mechanism. Results show that after specimens' suffering from the action of 20 NaCl D-As, the MR of ultra-high-performance concrete is the highest. Specimens exposed to 200 NaCl F-Cs show the lowest MR and CMC. The RME of UHPC under salt actions increase in the order of 20 NaCl D-As < 20 Na_2SO_4 D-As < 200 NaCl F-Cs. After suffering 200 NaCl F-Cs, 20 Na_2SO_4 D-As and 20 NaCl D-As, the corresponding D_c values are 1.86 mm to 2.31 mm, 1.79 mm to 2.23 mm and 2.11 mm to 2.76 mm. The flexural strength decreases at the rates of 0.99%–25%, 3.92%–27.84% and 1.47%–21.59% respectively. The MR increases and the RME decreases as the cubic function changes with the amount of salt erosion. After the secondary aluminum dross is added, the CMC decreases at the rates of 0% to 11.53%, 0% to 33.17% and 0% to 8.41% during the process of the salt action. The SAD can reduce the D_c with the decreasing rates of 19.48%, 23.55% and 19.73%. The SAD can increase the compactness of ultra-high-performance concrete. Ultra-high-performance concrete suffering from 20 NaCl D-As shows the largest number and the highest width of cracks. However, when the specimens are exposed to 20 Na_2SO_4 D-As, the number of cracks is the lowest and the width is the narrowest.

Keywords: secondary aluminum dross; salt erosion; mechanical strengths; dynamic modulus of elasticity; mechanical mechanism

1. Introduction

The generation and accumulation of solid waste in today's society are relatively complex environmental problems that trouble human beings [1]. Considering that the landfill deposits of this material will cause serious pollution to the environment, the solidification technology of solid waste appears to be very necessary [2,3]. The solidification technology of solid waste includes their use in concrete and the solidification effect of CO_2 applied for the disposal of the solid waste [4,5].

Secondary aluminum dross (SAD) is a by-product of aluminum production, causing environmental pollution if its treatment is not reasonable. The SAD possesses a large content of active oxide, which is beneficial to cement hydration. The use of SAD in cement-based materials can solidify the SAD to achieve the purpose of reducing its environmental pollution. Several studies have centered on the usage of SAD in cement concrete [6–9]. Satish found that SAD can increase the flexural and compressive strengths by 28.6% and

21.5%, respectively [10]. Moreover, SAD can decrease the chloride ion migration coefficient by 13.2% to 33.1% [11–14]. However, the concrete structure is usually exposed to various erosive environments. In a coastal environment, the erosion of NaCl and Na_2SO_4 accelerates the deterioration of concrete performance. Therefore, cement concrete materials in coastal environments require a high durability. The ultra-high-performance concrete (UHPC) showing excellent strength and durability can be used in salt erosion environments.

The UHPC is composed of continuous graded quartz sand, cement and a large amount of mineral admixtures [15,16]. This material is manufactured through the maximum density theory. Compared with other cement concrete, UHPC has the least pores and excellent mechanical and durable properties. Several researchers have found the positive effect of solid waste ash in UHPC's strength and durability. The solid waste ash and stove ash can increase the corresponding flexural strengths by the maximum rates of 23.4% and 17.1%, while the compressive strengths are increased by the maximum rates of 14.1% and 16.7% [17–19]. Additionally, the corrosion resistance of a reinforced UHPC matrix subjected to NaCl action is also improved by adding SAD [20–22]. In coastal environments, the mechanical performance can deteriorate when subjected to salt erosion. However, the SAD–UHPC's mechanical performance under the environment of salt erosion has not been investigated.

In this study, the flexural and compressive strengths (f_t and f_{cu}) of SAD–UHPC are measured. The NaCl F-C, NaCl D-A and Na_2SO_4 D-A actions on the specimens' mass loss rates (MRs), relative dynamic moduli of elasticity (RDMEs), carbonation depths and chloride ion permeabilities are studied. The scanning electron microscope (SEM) photos, energy dispersive spectrometer (EDS), thermogravimetric analysis (TG), X-ray diffraction spectrum (XRD) and mercury intrusion porosimetry (MIP) are utilized for the analysis of the mechanical mechanisms after NaCl and Na_2SO_4 action. This paper will offer theoretical supports for the application of SAD–UHPC in salt erosion environments.

2. Experimental Section

2.1. Raw Materials

Ordinary Portland cement (OPC) with the initial and final setting times of 103.1 min and 413.2 min purchased from the Ningguo cement plant of Anhui Conch Cement Co., Ltd., Ningguo city, China is used. The density of the OPC is 3.03 g/cm^3. Zhejiang Yongji Metal Materials Technology Co., Ltd., Jinhua, China offers the SAD for this research. The density of the SAD is 1.21 g/cm^3. The contents of AlN, Al_4C_3, AlP, Al_2S_3 and Al_5O_6N of the SAD are 0.03%, 0.01%, 0.02%, 0.025% and 0.013% of the total mass of the SAD. Other chemical compositions are shown in Table 1. Taiyue Mining (Shandong) Co., Ltd., Jinan, China, offers the ultra-fine fly ash (FA) used as the mineral admixture. The FA has a density of 2.45 g/cm^3 and particle diameters of 0.005 mm to 0.05 mm. Henan Tengze Environmental Technology Co., Ltd., Zhengzhou, China produces the quartz sand (QS) as aggregate for the UHPC. Efficient polycarboxylic acid water-reducing agent bought from Jilin Zhongxin New Building Materials Co., Ltd., Changchun, China, is used for the adjustment of the fresh UHPC's fluidity. The aggregates' particle sizes range from 3.21 to 1.57 mm, 0.83 to 0.33 mm, and 0.31 to 0.21 mm, respectively, with the corresponding mass ratio of 1:1:5:1 applied. Tables 1 and 2 show the accumulated pass ratios and the chemical compositions.

Table 1. Chemical composition (%).

Types	SiO$_2$	Al$_2$O$_3$	Fe$_x$O$_y$	MgO	CaO	SO$_3$	K$_2$O	Na$_2$O	Ti$_2$O	Loss on Ignition
OPC	20.3	5.8	3.9	1.9	62.2	2.8	-	-	-	3.1
FA	90.40	0.33	0.62	0.35	0.42	0.21	7.49	-	-	-
QS	98.7	-	1.3	-	-	-	-	-	-	-
SAD	4.7	79.2	4.3	5.2	1.6	-	-	0.9	-	3.8

Table 2. The accumulated pass rate (%).

Types	Particle Size/μm						
	0.3	0.6	1	4	8	64	360
OPC	0.13	0.36	3.1	14.8	29.2	92.8	100
FA	32.11	59.12	83.16	100	100	100	100
QS	0	0	0	0	0.035	24	100
SAD	0.04	0.31	0.55	1.11	3.95	25.4	88.13

2.2. The Preparing of Specimens

The binder materials (OPC, BFS, SF and SAD) are mixed uniformly in the NJ-160A mixer (Shanghai Meiyu Instrument Technology Co., Ltd., Shanghai, China) with a stirring speed of 60 rpm. After this mixing, the water and water-reducing agent are added to the mixer, stirring at the speed of 80 rpm for another 3 min. Then, the specimens with sizes of $40 \times 40 \times 160$ mm^3, $\Phi 100 \times 50$ mm^3 and $100 \times 100 \times 100$ mm^3 are manufactured. After curing in the environment (relative humidity of 40% and temperature of 20 ± 2 °C) for 1 day, the specimens are moved to an environment of 20.3 °C and 96.2% relative humidity for 23 days. The mixing proportions are shown in Table 3, which are used for manufacturing UHPC specimens. In this paper, six samples are prepared for each experiment. The average of the measured values is used as the testing result. The coefficient of variation of all experimental test data in this article is less than 0.1, ensuring the accuracy of the study.

Table 3. The mixing proportions of UHPC (kg/m^3).

Samples	Water	OPC	SAD	FA	QS	WR
SAD-0%	241.2	843.3	0	365.5	965.4	16.1
SAD-25%	241.2	843.3	91.4	274.1	965.4	16.1
SAD-50%	241.2	843.3	182.8	182.8	965.4	16.1
SAD-75%	241.2	843.3	274.1	91.4	965.4	16.1
SAD-100%	241.2	843.3	365.5	0	965.4	16.1

2.3. The NaCl F-C Action

A 3% NaCl solution is used for immersing specimens for 4 days. After the immersion, specimens are moved to the TDS-300 fully automatic rapid freeze–thaw test box provided by Nanjing Annai Testing Equipment Co., Ltd., Nanjing, China, for the experiment. Specimens are moved to the sealed stainless-steel freeze–thaw boxes filled with the NaCl solution at the same concentration. The temperature in the F-C box ranges from -15 °C to 8 °C. The freezing time of each F-C is 2–3 h, while the thawing time of each F-C is 1–2 h. All parameters are determined for each of the 50 NaCl F-Cs. Figure 1 shows the process of the NaCl F-C.

Figure 1. The experiment of quick freeze–thaw action.

2.4. The NaCl and Na$_2$SO$_4$ D-A Actions

The immersion process of specimens in NaCl is the same as the NaCl F-C action. After the immersion, the specimen are moved to the concrete corrosion-resistant dry–wet cycle testing machine bought from Tianjin Huida Experimental Instrument Co., Ltd., Tianjin, China for the experiment of NaCl D-A. During each D-A, 8 hours of solution immersion in NaCl or Na$_2$SO$_4$ are applied to the specimens; after that, the surfaces of the specimens are dried using a rag. Then, the specimens are dried at a temperature of 80 °C for 36 h. Ultimately, the samples are cooled for 2 h. Figure 2 shows the process of Na$_2$SO$_4$ D-A.
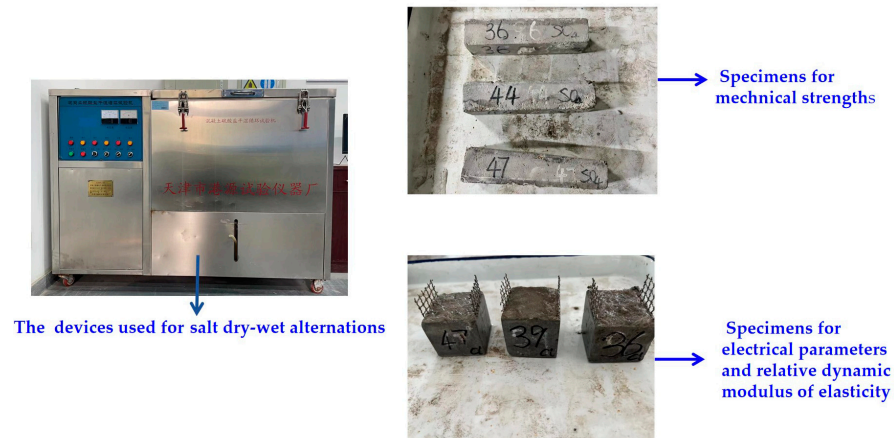

Figure 2. The experiment of Na$_2$SO$_4$ D-A action.

2.5. The Measurement of MR

Specimens' masses are determined after the specimens are immersed in NaCl for 4 days. After that, the specimens' surfaces are wiped. Then, the masses of the specimens are determined using the DH-8905 electronic scale manufactured by Dongguan Dingheng Electronics Co., Ltd., Dongguan, China, with the measurement range of 0–3 kg and the minimum accuracy of 0.1 g. The *MR* can be calculated with Equation (1),

$$MR = \frac{m_t - m_1}{m_1} \tag{1}$$

where m_1 is the mass of the specimen after the 4-day immersion in 3% NaCl solution and m_t is the mass of the specimen after 50 F-Cs or 10 D-As.

2.6. The Measurement of the Relative Dynamic Modulus of Elasticity

A HS600 digital ultrasonic flaw detector manufactured by Shanxi Gangyan Testing Technology Co., Ltd., Taiyuan, China, is used for the determination of the relative dynamic modulus of elasticity (*RDEM*). The probes of the receiving and transmitting ends of the ultrasound are tightly adhered to the center positions of the specimens. The baseline is used for the match between the probes and the specimens. The *RDEM* is calculated by Equation (2),

$$RDEM = \left(\frac{v_t}{v_1}\right)^2 \tag{2}$$

where v_1 and v_t are the ultrasonic velocities of the specimens after 4 days of NaCl or Na$_2$SO$_4$ immersion and each 50 NaCl F-Cs, 10 NaCl D-As or 10 Na$_2$SO$_4$ D-As. Specimens with sizes of $100 \times 100 \times 100$ mm^3 are used for the measurements of *MR* and *RDEM*. The flowchart of the experimental process is shown in Figure 3.
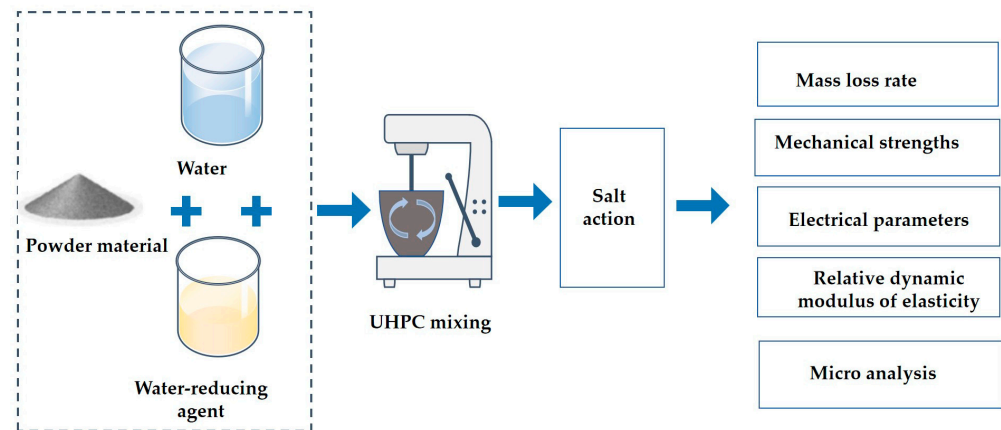
Figure 3. The flowchart of the experimental process.

2.7. The Measurement of Mechanical Strengths

The flexural strength (f_t) and compressive strength (f_{cu}) are determined with the fully automatic bending and integrated testing machine (Shanghai Qunhong Instrument Equipment Co., Ltd., Shanghai, China) with the loading rates of 0.05 kN/s and 2.4 kN/s, respectively. The mechanical strength measurements are carried out with specimens of the size $40 \times 40 \times 160$ mm^3.

2.8. The Chloride Ion Migration Coefficient

The CMC of the UHPC is measured with the RCM-6 concrete chloride ion diffusion coefficient tester manufactured by Shanghai Shengshi Huike Testing Equipment Co., Ltd., Shanghai, China. All specimens are firstly processed with the vacuum saturation treatment and then moved to the measurement of the CMC. The vacuum saturation machine (Shanghai Shengshi Huike Testing Equipment Co., Ltd., Shanghai, China) with a vacuum volume of 18 L and accuracy of 0.1% is used for the vacuum saturation. A concrete chloride ion diffusion coefficient tester (Cangzhou Taiding Hengye Testing Instrument Co., Ltd., Cangzhou, China) with the measuring voltages of 10 V to 60 V and a voltage accuracy of 0.1 V is used for measuring the CMC.

2.9. The Carbonation Depth

The carbonation depth (D_c) of UHPC is determined after treatment in the TH-2 concrete carbonization test box (Hebei Zhongyi Weichuang Test Instrument Co., Ltd., Cangzhou, China). The detailed testing process can be described as follows:

The UHPC specimens are placed into the carbonization box. The concentration of the CO_2 in the carbonization box is $20 \pm 3\%$. The temperature and the humidity in the carbonization box are 20 ± 5 °C and $70 \pm 5\%$. After the specimens are cured in the carbonization box for 28 days, the specimens are taken out and broken to determine their carbonization depth. The specimens are cut off by half of their width. The remaining powder on the section of the cut specimen is scraped off, and then a 1% concentration of phenolphthalein alcohol solution (containing 20% evaporated water) is sprayed. After 30 s, the carbonization depth of each point on both sides at every 10 mm marked previously is measured in a carbonization depth test box. In this paper, the variation coefficients of all macroscopic performance experimental results are lower than 0.1.

2.10. The SEM Experiment

The samples' inner UHPC with the diameter of 0.5 mm to 1 mm is used for the experiment of SEM. All samples are dried in the vacuum oven at 105 °C for 2 days. The samples are coated with gold until dry. Finally, the samples coated with gold are moved to the SEM to obtain the photos magnified 10,000 times.

3. Results and Discussions

3.1. The MR of UHPC

In this paper, the *N* of all fitting equations presents the amount of salt action. *a*, *b*, *c* and *d* represent the *MR* of specimens with the increasing numbers of NaCl F-Cs, NaCl D-As and Na$_2$SO$_4$. Figure 4 displays the *MR* of the UHPC exposed to erosion action. The *MR* of specimens increases with the increasing number of NaCl F-Cs, NaCl D-As and Na$_2$SO$_4$ D-As. The NaCl F-Cs can increase the frost-heaving stress and crystallization stress inside the UHPC [23,24], thus, accelerating the surface peeling on UHPC. Therefore, the *MR* increases with the NaCl F-C action. The NaCl D-A can increase the crystalline stress of the UHPC; hence, the surface peeling on the UHPC is exacerbated, resulting in the increased *MR* of UHPC [25]. Additionally, the chloride accelerates the alkali aggregate reaction of UHPC, which increases the mass loss of the UHPC. Meanwhile, the dry–wet cycling of sulfate acts on the UHPC, the internal cementitious material undergoes a chemical reaction with sulfate and decomposes to form an erosion product, ettringite, which appears inside the UHPC. While the quantity of SAD increases, the *MR* of UHPC decreases. This can be ascribed to the reason that the SAD can form an aluminum hydroxide gel with cement, thus making UHPC more compact; therefore, the resistance to salt erosion is enhanced [26–29]. The *MR* of UHPC is the highest after suffering NaCl D-As, while the UHPC after suffering the NaCl F-Cs shows the lowest *MR*. The relationships between the number of NaCl F-C, NaCl D-A and Na$_2$SO$_4$ actions and the *MR* fit with the function of Equation (3). Table 4 shows the fitting equations of the relationships between the amount of erosion action and the *MR*. The R-squared is higher than 0.98, which ensures the rationality of fitting equations. After 200 NaCl F-Cs, 20 Na$_2$SO$_4$ and 20 NaCl D-As, the *MR* of UHPC are 0.76% to 1.47%, 1.24% to 1.97% and 1.42% to 2.14%, while the *MR* are decreased at the decreasing rates of 0% to 48.2%, 0% to 33.6% and 0% to 37.1% by adding the SAD.
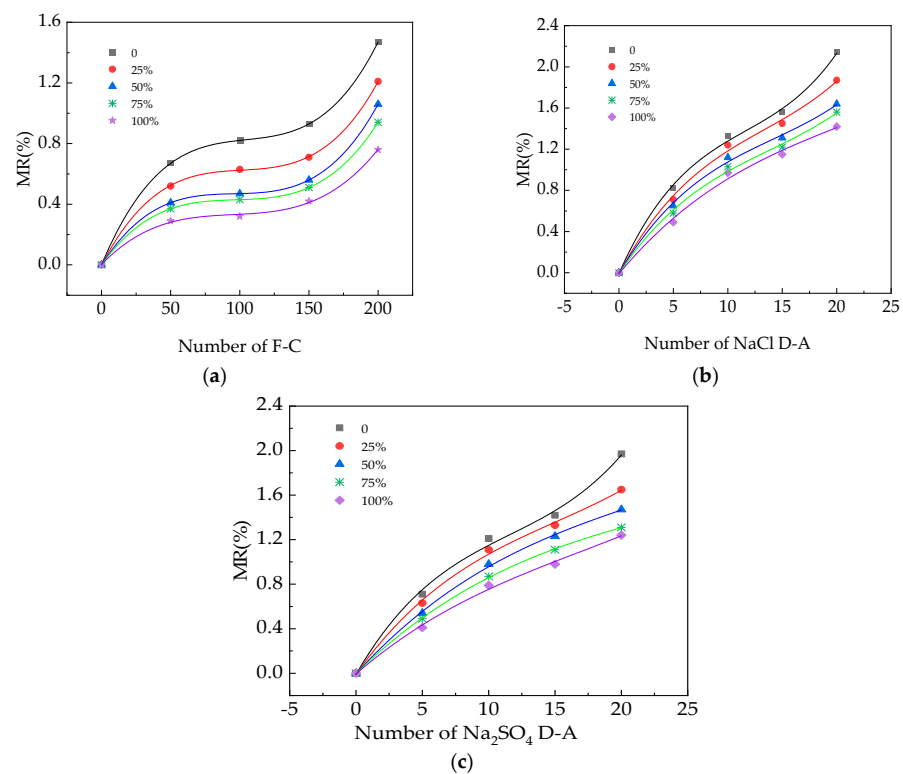
$$MR = aN^3 + bN^2 + cN + d \qquad (3)$$

Figure 4. The MR of UHPC exposed to erosion action. (**a**) NaCl F-C action. (**b**) NaCl D-A action. (**c**) Na$_2$SO$_4$ D-A action.

Table 4. The fitting equations of the relationship between the amount of erosion action and the *MR*.

Equation Types	SAD Content	a	b	c	d	R^2
NaCl F-C	0%	6.33×10^{-7}	-1.96×10^{-4}	2.17×10^{-2}	1.42857×10^{-4}	0.99
	25%	5.58×10^{-7}	-1.75×10^{-4}	1.75×10^{-2}	-1×10^{-3}	0.99
	50%	5.12×10^{-7}	-1.51×10^{-4}	1.42×10^{-2}	-1.99×10^{-16}	1.00
	75%	4.44×10^{-7}	-1.28×10^{-4}	1.27×10^{-2}	-5.96×10^{-16}	1.00
	100%	3.33×10^{-7}	-9.51×10^{-5}	9.5×10^{-3}	2.29×10^{-3}	0.98
NaCl D-A	0%	4.40×10^{-4}	-1.54×10^{-2}	2.38×10^{-1}	-8.57×10^{-3}	0.99
	25%	2.60×10^{-4}	-1.04×10^{-2}	1.97×10^{-1}	-9.57×10^{-3}	0.98
	50%	2.13×10^{-4}	-9.03×10^{-3}	1.77×10^{-1}	-7.43×10^{-3}	0.99
	75%	1.87×10^{-4}	-7.71×10^{-3}	1.58×10^{-1}	-7.71×10^{-3}	0.99
	100%	6.67×10^{-5}	-4.11×10^{-3}	1.27×10^{-1}	-9.71×10^{-3}	0.98
Na$_2$SO$_4$ D-A	0%	3.67×10^{-4}	-1.27×10^{-3}	0.21	-1.01×10^{-2}	0.99
	25%	1.67×10^{-4}	-7.51×10^{-3}	0.17	-6.71×10^{-3}	0.99
	50%	6.00×10^{-5}	-4.06×10^{-3}	0.13	-3.86×10^{-3}	0.99
	75%	4.67×10^{-5}	-3.46×10^{-3}	0.12	-1.86×10^{-3}	0.99
	100%	6.67×10^{-5}	-3.40×10^{-3}	0.10	-6×10^{-3}	0.98

3.2. The RDME of UHPC

Figure 5 shows the RDME of UHPC after suffering different numbers of NaCl F-C, NaCl D-A and Na$_2$SO$_4$ D-A actions. The RME of UHPC decreases with increased NaCl F-C, NaCl D-A and Na$_2$SO$_4$ D-A numbers. The frost heaving-stress stemming from NaCl F-Cs and the crystalline stress generated by NaCl F-Cs and NaCl D-As can facilitate the development and number of cracks inside the UHPC. The cracks obstruct the propagation of ultrasounds, resulting in a decrease in the *RDEM* [30,31]. When the UHPC undergoes the Na$_2$SO$_4$ erosion, the internal UHPC is exposed to a chemical reaction with sulfate and decomposes to form an erosion product, ettringite, leading to more cracks in the specimens. The erosion product expands, and the voids are irregularly distributed in the mortar. The presence of these voids will gradually deteriorate the *RDEM* of the mortar. The amount of salt erosion shows the cubic function with the RME, which is shown in Equation (4). Table 5 shows the fitting equations of the relationships between the amount of erosion action and the RDEM. The R-squared of the fitting curves are higher than 0.98. However, the RME is increased by adding SAD. Due to the improved compactness and decreased inner cracks, the ultrasound's speed is increased [32,33]. Therefore, the addition of SAD increases the RME. Meanwhile, the RME of UHPC is the highest after 200 NaCl F-Cs. The UHPC shows the lowest *RDEM* after suffering 20 NaCl D-As, due to the most serious erosion action of NaCl D-As on the UHPC. After 200 NaCl F-Cs, 20 Na$_2$SO$_4$ and 20 NaCl D-As, the RMEs of UHPC are 89.7% to 95.3%, 89.4% to 95.7% and 86.3% to 94.8%. Additionally, the SAD can increase the *RDEM* with the increasing rates of 5.88%, 8.97% and 6.58%.

$$RDEM = aN^3 + bN^2 + cN + d \tag{4}$$

Table 5. The fitting equations of the relationships between the amount of erosion action and the *RDEM*.

Equation Types	SAD Content	a	b	c	d	R^2
NaCl F-C	0%	1.00×10^{-6}	-1.14×10^{-4}	-6.86×10^{-2}	99.98	0.99
	25%	1.93×10^{-6}	-5.49×10^{-4}	-1.21×10^{-2}	99.97	0.99
	50%	8.67×10^{-7}	-3.03×10^{-4}	-1.26×10^{-2}	99.98	0.99
	75%	-8.67×10^{-7}	1.34×10^{-4}	-2.47×10^{-2}	100.02	0.99
	100%	-2×10^{-7}	-1.43×10^{-5}	-1.26×10^{-2}	100.02	0.99

Table 5. *Cont.*

Equation Types	SAD Content	a	b	c	d	R^2
NaCl D-A	0%	-4.67×10^{-4}	-2.69×10^{-2}	-1.04	99.98	0.99
	25%	1.73×10^{-3}	-4.43×10^{-2}	-0.33	99.97	0.99
	50%	6.00×10^{-4}	-1.77×10^{-2}	-0.33	100.02	0.99
	75%	-1.13×10^{-3}	2.49×10^{-3}	-0.41	100.03	0.99
	100%	1.33×10^{-4}	-8.29×10^{-3}	-0.15	100.01	0.99
Na$_2$SO$_4$ D-A	0%	1.20×10^{-3}	-0.02	-0.61	99.94	0.99
	25%	2×10^{-3}	-0.06	-0.09	99.94	0.99
	50%	1×10^{-3}	-0.03	-0.14	100.02	0.99
	75%	-6×10^{-4}	0.01	-0.24	100.04	0.98
	100%	2×10^{-4}	-0.01	-0.06	100.01	0.99
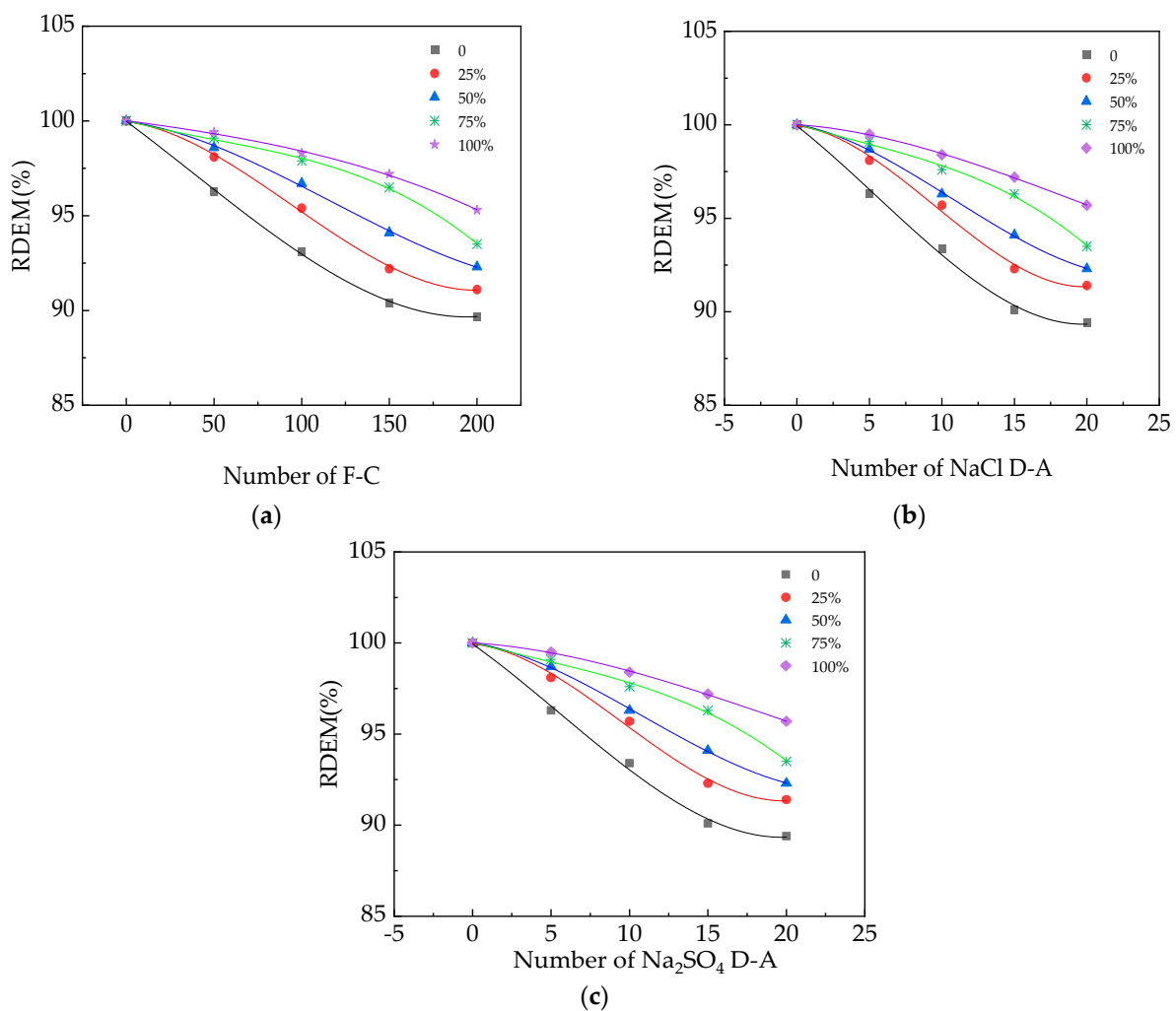
Figure 5. The RDEM of UHPC exposed to erosion action. (**a**) NaCl F-C action. (**b**) NaCl D-A action. (**c**) Na$_2$SO$_4$ D-A action.

3.3. The Mechanical Strengths of UHPC

The f_t of UHPC after suffering from different types of salt erosion are shown in Figure 6. The f_t of UHPC decreases with the number of NaCl F-Cs, NaCl D-As and Na$_2$SO$_4$ D-As, due to the reason that the salt erosion can increase the number and widen the size of cracks in UHPC, decreasing the f_t. As found in Figure 6, the UHPC after NaCl D-A action shows the lowest f_t. However, when the mixed content of SAD is increased, the f_t of the UHPC

is increased. The SAD can increase the amount of aluminum hydroxide, which makes the hydration products more compact [34,35]. Hence, the f_t is improved by adding SAD. The f_t of UHPC after NaCl F-C action is the highest, while the f_t of UHPC is the lowest after suffering from NaCl D-A erosion. After 200 NaCl F-Cs, 20 Na_2SO_4 and 20 NaCl D-As, the f_t of UHPC decreases with the decreasing rates of 0.99%–25%, 3.92%–27.84% and 1.47%–21.59%. The SAD can increase the f_t by 0%–23.4%, 0%–25.1% and 0%–13.4%.
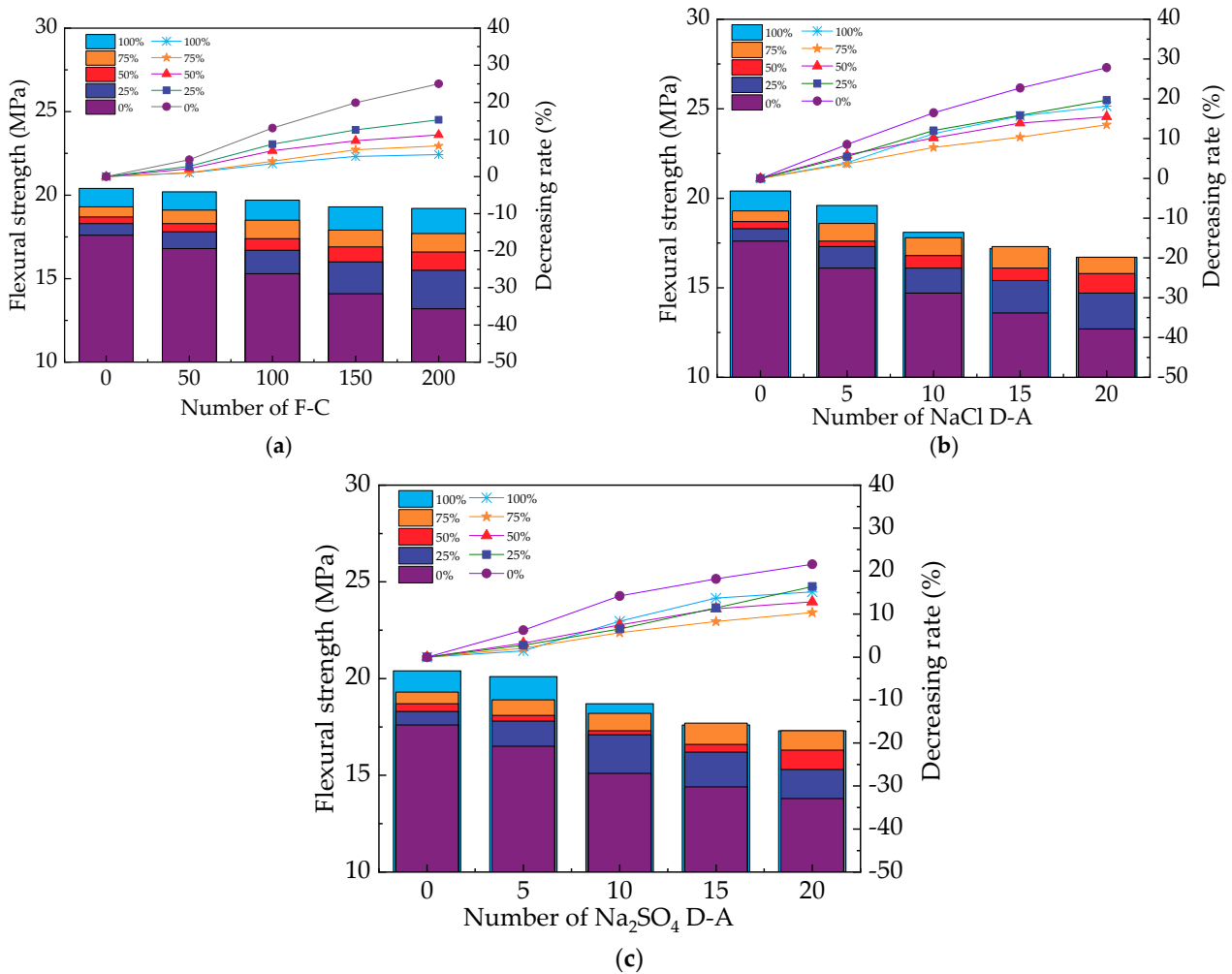
Figure 6. The flexural strengths of UHPC under erosion action. (**a**) NaCl F-C action. (**b**) NaCl D-A action. (**c**) Na_2SO_4 D-A action.

Figure 7 shows the f_{cu} of UHPC after suffering from different types of salt erosion. It can seen in Figure 7 that similar varying levels of f_{cu} and f_t occur. The f_{cu} shows an increasing trend with the increasing quantity of SAD and a decreasing trend with the number of NaCl F-Cs, NaCl D-As and Na_2SO_4 D-As. The reasons for these results are the same with the f_t's results [36,37]. The relationship between the number of NaCl F-Cs, NaCl D-As and Na_2SO_4 D-As and the f_{cu} coincides with the cubic function. The UHPC demonstrates the highest compressive strength when exposed to the NaCl F-C environment. However, the f_{cu} of UHPC is the lowest after suffering 20 NaCl D-As. After 200 NaCl F-Cs, 20 Na_2SO_4 and 20 NaCl D-As, the f_{cu} of UHPC decreases with the decreasing rates of 1.59%–10.31%, 3.09%–11.45% and 1.63%–9.62%. After the SAD is added, the f_{cu} of UHPC increases to 4.13%–21.16%, 5.41%–22.76% and 5.53%–21.41%.
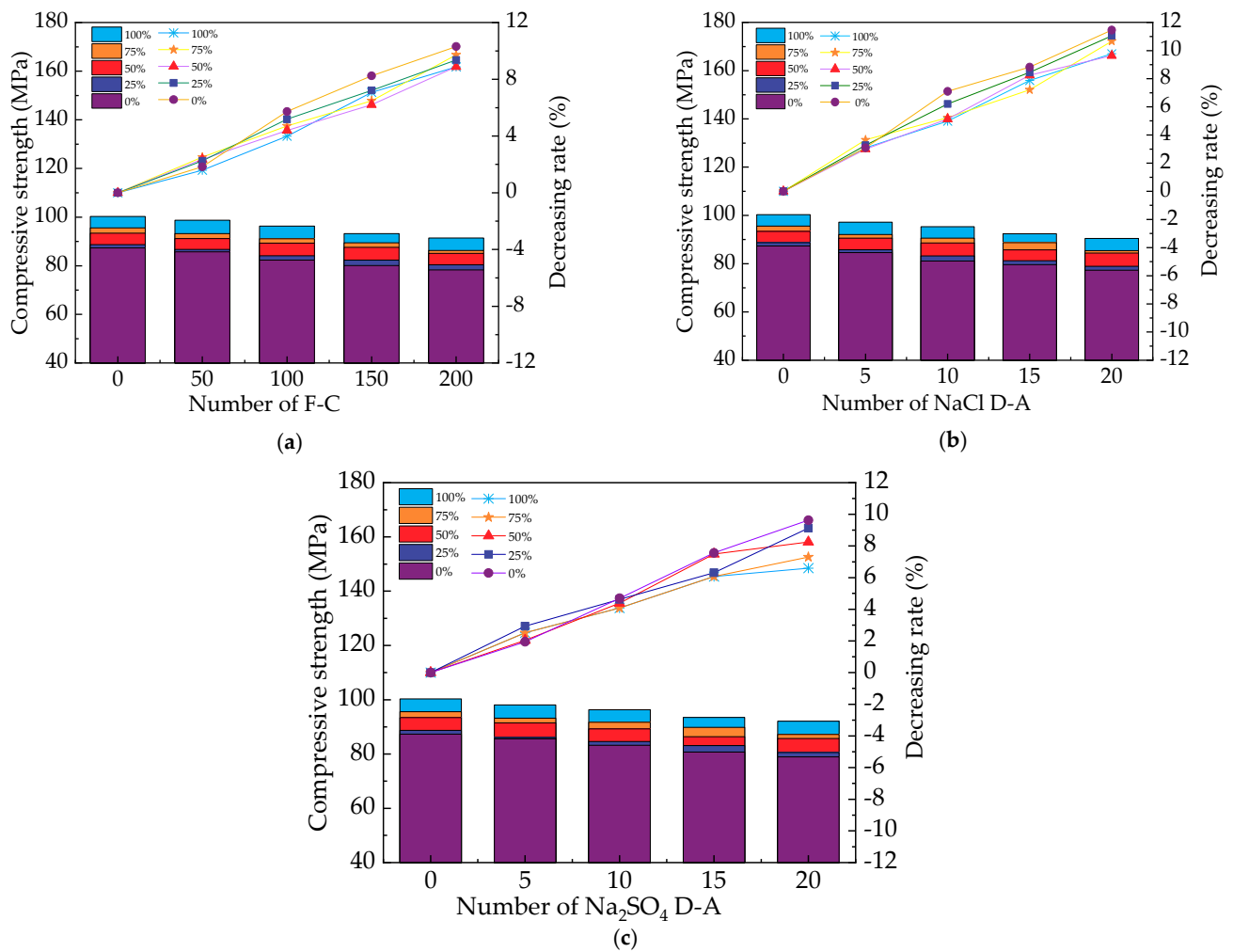
Figure 7. The compressive strength of UHPC exposed to erosion action. (**a**) NaCl F-C action. (**b**) NaCl D-A action. (**c**) Na$_2$SO$_4$ D-A action.

3.4. The CMC of UHPC

The CMC curves of the UHPC after suffering from different NaCl F-Cs, Na$_2$SO$_4$ and NaCl D-As are shown in Figure 8. The CMC of UHPC increases with the increased numbers of NaCl F-Cs and Na$_2$SO$_4$ and NaCl D-As, which is attributed to the cracking number and width [38,39]. The chloride ions migrate along the cracks, thereby increasing the CMC. The increasing quantity of SAD decreases the CMC of the UHPC, due to the improved compactness with the addition of SAD, which prevents the chloride ions from migrating along the cracks, thereby reducing the CMC. The relationships between the amount of salt erosion activity and the CMC fit the model of the cubic function shown in Equation (5). Table 6 shows the fitting equations of the relationships between the amount of erosion activity and the CMC. The R-squared of the fitting equations is higher than 0.91. After suffering 200 NaCl F-Cs and 20 Na$_2$SO$_4$ and 20 NaCl D-As, the CMCs are 3.68×10^{-12} m^2/s to 4.16×10^{-12} m^2/s, 3.59×10^{-12} m^2/s to 3.92×10^{-12} m^2/s and 4.03×10^{-12} m^2/s to 6.03×10^{-12} m^2/s. As established by the results, the CMC is the highest after treatment with 20 NaCl D-As. However, the CMC is the lowest after being exposed to 20 Na$_2$SO$_4$ D-As. The NaCl D-As can cause UHPC cracking the most seriously, simultaneously increasing the concentration of chloride ions in the UHPC pore solution. Therefore, the CMC of UHPC is the highest after the action of 20 NaCl D-As. However, the Na$_2$SO$_4$ D-A action induces the lowest number and width of cracks and cannot introduce chloride ions. Hence, the CMC of UHPC with 20 Na$_2$SO$_4$ D-As is the lowest. After the salt

action, the CMC are decreased, with rates of 0% to 11.53%, 0% to 33.17% and 0% to 8.41% by adding SAD. As observed in Sections 3.1–3.4, when the addition of MS is 100% (30% of the total binder materials), the resistance of the NaCl and Na$_2$SO$_4$ dry–wet alternations are the highest, which is ascribed to the pozzolanic effect.
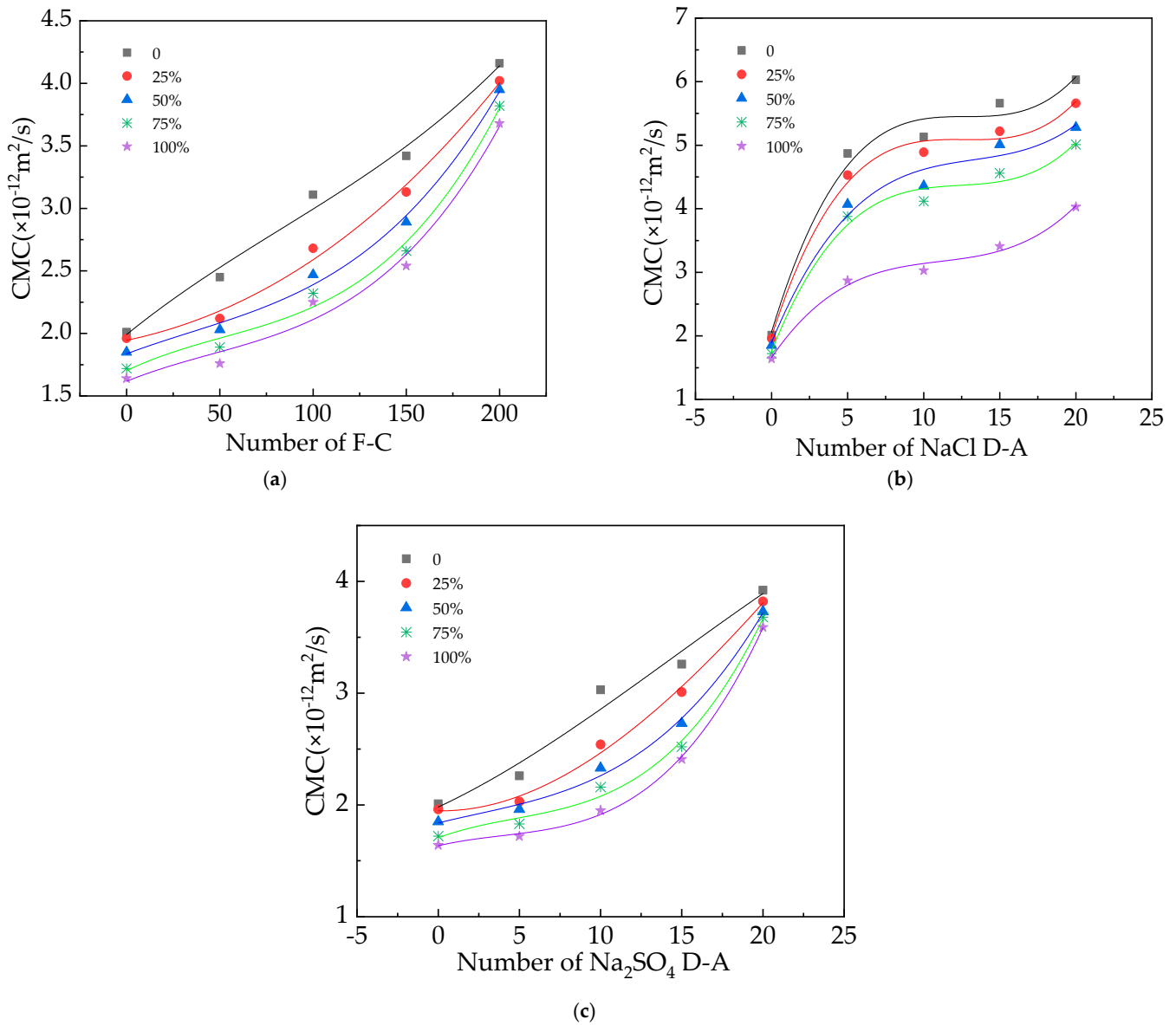
$$CMC = aN^3 + bN^2 + cN + d \tag{5}$$

Figure 8. The CMC of UHPC exposed to erosion action. (**a**) NaCl F-C action. (**b**) NaCl D-A action. (**c**) Na$_2$SO$_4$ D-A action.

Table 6. The fitting equations of the relationship between the amount of erosion action and the CMC.

Equation Types	SAD Content	a	b	c	d	R^2
NaCl F-C	0%	1.4×10^{-7}	-3.49×10^{-5}	1.21×10^{-2}	1.99	0.96
	25%	2.67×10^{-8}	3.06×10^{-5}	3.12×10^{-3}	1.94	0.98
	50%	2.53×10^{-7}	-2.63×10^{-5}	5.62×10^{-3}	1.84	0.98
	75%	3.73×10^{-7}	-5.8×10^{-5}	7.17×10^{-3}	1.70	0.97
	100%	3.2×10^{-7}	-4.34×10^{-5}	6.09×10^{-3}	1.62	0.94

Table 6. *Cont.*

Equation Types	SAD Content	a	b	c	d	R^2
NaCl D-A	0%	1.63×10^{-3}	-0.06	0.80	2.06	0.94
	25%	1.55×10^{-3}	-0.06	0.74	1.99	0.97
	50%	1.03×10^{-3}	-0.04	0.58	1.89	0.93
	75%	1.29×10^{-3}	-0.05	0.61	1.75	0.95
	100%	8.73×10^{-4}	-0.03	0.35	1.66	0.97
Na$_2$SO$_4$ D-A	0%	-6.00×10^{-5}	2.6×10^{-3}	0.07	-1.98	0.91
	25%	-6.67×10^{-5}	6.11×10^{-3}	-2.62×10^{-3}	1.95	0.98
	50%	2.27×10^{-4}	-1.63×10^{-3}	3.59×10^{-2}	1.84	0.98
	75%	3.87×10^{-4}	-5.51×10^{-3}	0.05	1.71	0.98
	100%	3.8×10^{-4}	-4.46×10^{-3}	0.03	1.63	0.99

3.5. The Carbonation Depth of UHPC

Figure 9 exhibits the carbonation depth (D_c) of UHPC. The D_c shows the increasing trend with more occurrences of NaCl F-Cs and Na$_2$SO$_4$ and NaCl D-As, due to the increased cracks by the salt action [40]. The CO$_2$ can infiltrate into the interior of the UHPC along the crack, leading to an accelerated carbonation reaction, thereby increasing the depth of carbonation. The relationships between the amount of salt erosion action and D_c fit the model of the cubic function shown in Equation (6). Table 7 shows the fitting equations of the relationships between the amount of erosion action and the CMC. The R-squared of the fitting equations is higher than 0.91. After suffering from 200 NaCl F-Cs, 20 Na$_2$SO$_4$ and 20 NaCl D-As, the D_c values are 1.86 mm to 2.31 mm, 1.79 mm to 2.23 mm and 2.11 mm to 2.76 mm. The D_c is the highest after being treated with 20 NaCl D-As. This is ascribed to the most serious cracking by the NaCl D-As, which increases the D_c. However, the crack width and number induced by the Na$_2$SO$_4$ D-A action is the lowest, resulting in the lowest D_c. The addition of SAD can decrease the D_c, with the decreasing rates of 19.48%, 23.55% and 19.73%. It can be determined from Figure 9, that a UHPC with 100% MS (30% of the total binder materials) shows the optimum anti-carbonation and penetration performance.

$$D_c = aN^3 + bN^2 + cN + d \tag{6}$$

Table 7. The fitting equations of the relationships between the amount of erosion action and the D$_c$.

Equation Types	SAD Content	a	b	c	d	R^2
NaCl F-C	0%	1.8×10^{-7}	-5.89×10^{-5}	9.42×10^{-3}	1.34	0.99
	25%	8×10^{-8}	-2.86×10^{-5}	7.31×10^{-3}	1.21	0.99
	50%	-9.33×10^{-8}	2.49×10^{-5}	3.16×10^{-3}	1.15	0.95
	75%	-6.67×10^{-9}	8.57×10^{-7}	4.45×10^{-3}	1.07	0.97
	100%	-8.67×10^{-8}	2.91×10^{-5}	1.89×10^{-3}	1.00	0.98
NaCl D-A	0%	1.2×10^{-4}	-5.94×10^{-3}	0.14	1.35	0.98
	25%	-6.67×10^{-5}	4×10^{-4}	0.08	1.24	0.96
	50%	-1.8×10^{-4}	4.77×10^{-3}	0.04	1.18	0.91
	75%	-1×10^{-4}	-2×10^{-3}	0.06	1.10	0.93
	100%	-1.87×10^{-4}	4.89×10^{-3}	0.03	1.02	0.95
Na$_2$SO$_4$ D-A	0%	6.67×10^{-6}	-2.86×10^{-5}	0.04	1.33	0.96
	25%	-2×10^{-5}	2.86×10^{-5}	0.05	1.20	0.97
	50%	-6×10^{-5}	2.11×10^{-3}	0.02	1.15	0.97
	75%	-6×10^{-4}	5.37×10^{-3}	-6.6×10^{-3}	1.08	0.99
	100%	-1.47×10^{-4}	6.17×10^{-3}	-0.03	1.01	0.99

(**a**)


(**b**)

(**c**)
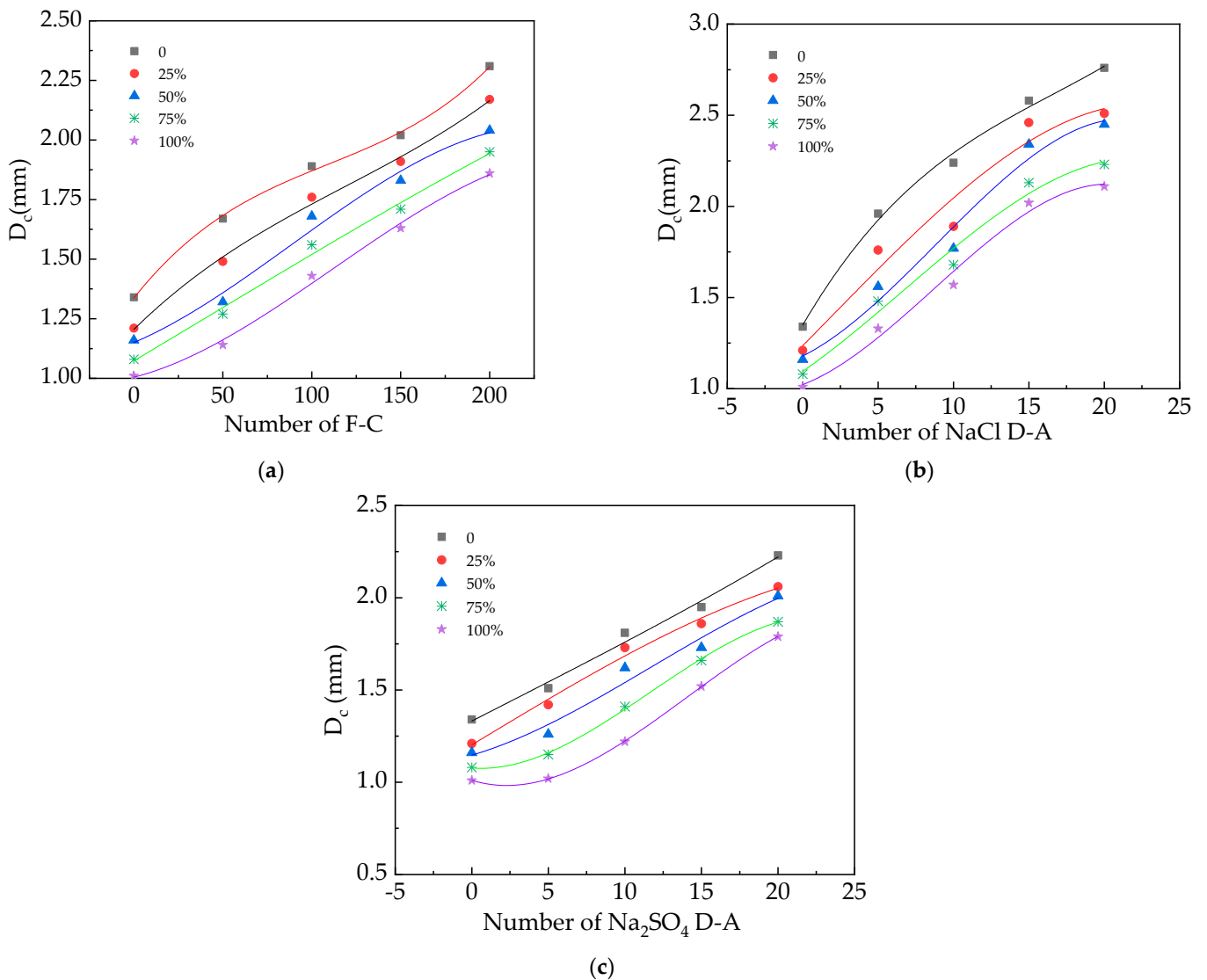
Figure 9. The D_c of UHPC exposed to erosion action. (**a**) NaCl F-C action. (**b**) NaCl D-A action. (**c**) Na_2SO_4 D-A action.
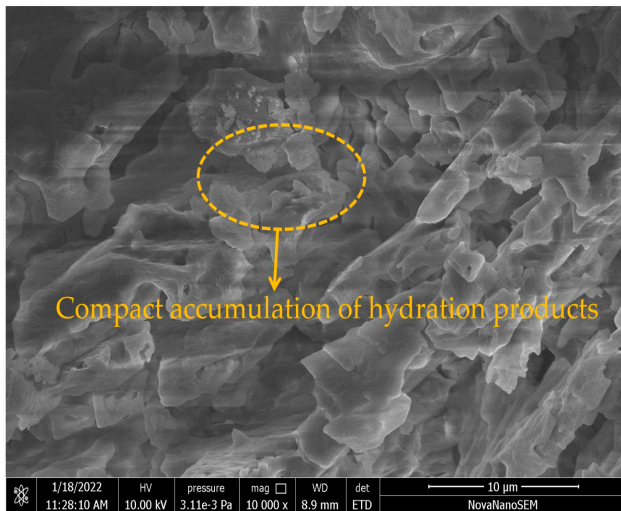
3.6. The SEM Photos of UHPC

The SEM pictures of the UHPC with 0%, 50% and 100% SAD are provided in Figure 10a–c. Moreover, the UHPC with 50% SAD exposed to 200 NaCl F-Cs, 20 Na_2SO_4 and 20 NaCl D-As are shown in Figure 10d–f. It can be observed in the photos that the rhombic hydration products decrease with the addition of SAD. With the increasing quantity of SAD, the hydration products become more compact. Some cracks are found in the SEM photos. The UHPC shows a higher number and wider cracks after 20 NaCl D-As. Meanwhile, the cracks are the lowest when the UHPC suffers from 20 Na_2SO_4 D-As.
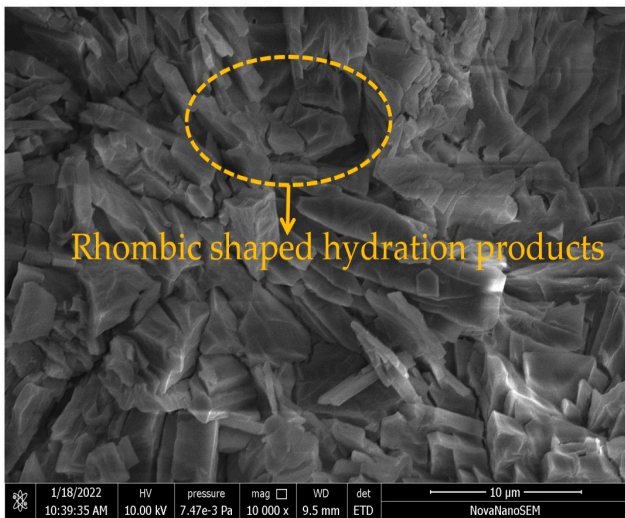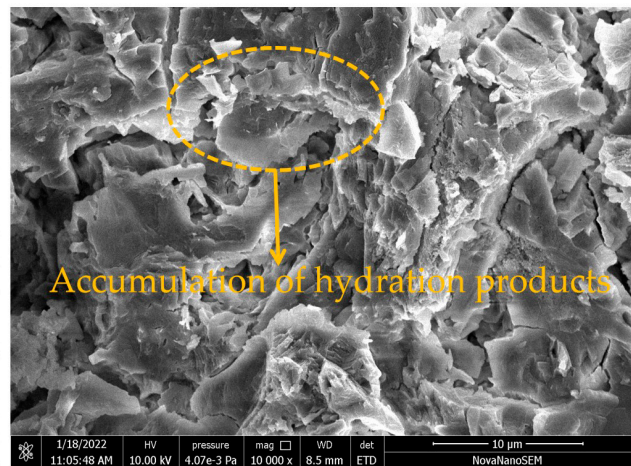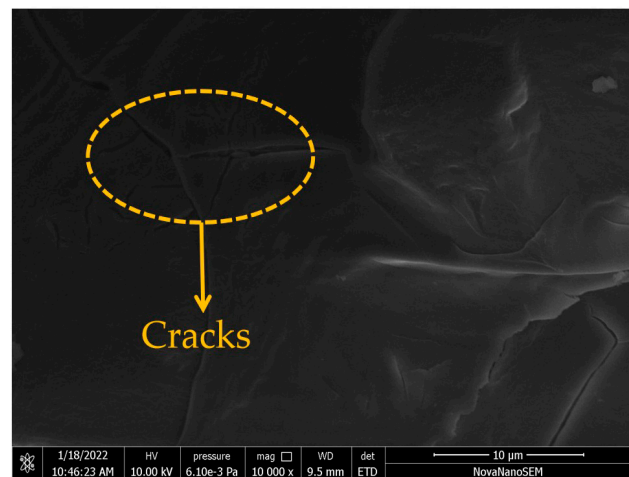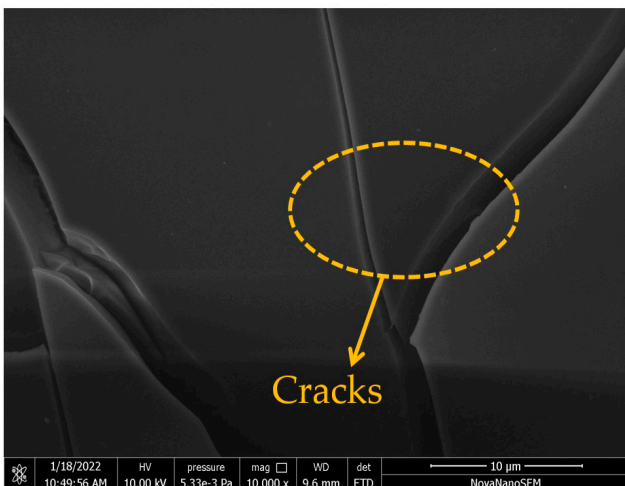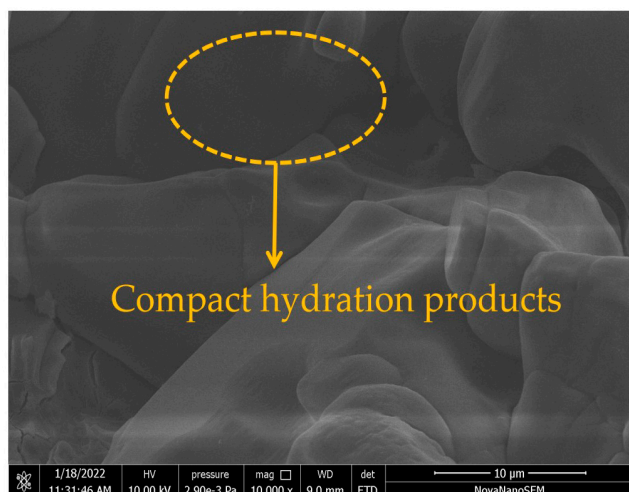
Figure 10. The SEM photos of UHPC exposed to erosion action. (**a**) UHPC with 0% SAD. (**b**) UHPC with 50% SAD. (**c**) UHPC with 100% SAD. (**d**) UHPC with 50% SAD after NaCl F-C. (**e**) UHPC with 50% SAD after NaCl D-A. (**f**) UHPC with 50% SAD after Na$_2$SO$_4$ D-A.

4. Conclusions

The paper aims to investigate the attenuation of mechanical properties after suffering salt erosion. The conclusions are as described below.

The MR of UHPC increases in the cubic function with NaCl F-C, NaCl D-A and Na_2SO_4 D-A numbers. After 200 NaCl F-Cs, 20 Na_2SO_4 and 20 NaCl D-As, the MR are 0.76% to 1.47%, 1.24% to 1.97% and 1.42% to 2.14%.

The UHPC's RME decreases in the cubic function with more rounds of NaCl F-Cs, NaCl D-As and Na_2SO_4 D-As. After suffering from 200 NaCl F-Cs, 20 Na_2SO_4 and 20 NaCl D-As, the RMEs of UHPC are 89.7% to 95.3%, 89.4% to 95.7% and 86.3% to 94.8%.

The relationship between the CMC and D_c and the amount of salt action shows the cubic function. When 200 NaCl F-Cs, 20 Na_2SO_4 and 20 NaCl D-As are finished, the CMCs are 3.68×10^{-12} m^2/s to 4.16×10^{-12} m^2/s, 3.59×10^{-12} m^2/s to 3.92×10^{-12} m^2/s and 4.03×10^{-12} m^2/s to 6.03×10^{-12} m^2/s, while the corresponding D_c values are 1.86 mm to 2.31 mm, 1.79 mm to 2.23 mm and 2.11 mm to 2.76 mm.

The f_t and f_{cu} demonstrate decreasing trends with the NaCl F-C, NaCl D-A and Na_2SO_4 D-A actions. After 200 NaCl F-Cs, 20 Na_2SO_4 and 20 NaCl D-As, the flexural strengths of UHPC decrease with the decreasing rates of 0.99%–25%, 3.92%–27.84% and 1.47%–21.59%, while the f_{cu} of UHPC decreases with the decreasing rates of 1.59%–10.31%, 3.09%–11.45% and 1.63%–9.62%. The CMCs are decreased with the rates of 0% to 11.53%, 0% to 33.17% and 0% to 8.41% by adding SAD, after the salt action. The SAD can reduce the D_c with the decreasing rates of 19.48%, 23.55% and 19.73%.

UHPC with SAD shows an improved compact structure. After exposure to salt action, the UHPC that suffered from 20 NaCl D-As shows the largest number and highest width of cracks. However, when specimens are exposed to 20 Na_2SO_4 D-As, the number of cracks is the lowest and the width is the narrowest. When the mass ratio of SAD is 100% (30% of the total binder materials), the resistances of the UHPC's CO_2 penetration and NaCl and Na_2SO_4 dry–wet alternations are the best.

Author Contributions: Methodology, W.S., F.S., H.S. and H.W.; Software, H.S., F.S. and L.M.; Validation, H.S. and H.W.; Formal analysis, W.S.; Investigation, H.S. and F.S.; Resources, H.S.; Writing—original draft, H.S.; Writing—review & editing, H.W.; Project administration, H.W. All authors have read and agreed to the published version of the manuscript.

Institutional Review Board Statement: Not applicable.

Informed Consent Statement: Not applicable.

Data Availability Statement: Data are contained within the article.

Conflicts of Interest: Authors Weixiang Sun and Lu Miao were employed by the company China Construction Infrastructure Co., Ltd. The remaining authors declare that the research was conducted in the absence of any commercial or financial relationships that could be construed as a potential conflict of interest.

References

1. Cabrera Luna, K.; Maldonado Bandala, E.E.; Nieves Mendoza, D. Supersulfated binders based on volcanic raw material: Optimization, microstructure and reaction products. *Constr. Build. Mater.* **2018**, *176*, 145–155. [CrossRef]
2. Han, F.; Song, S.; Liu, J.; Huang, S. Properties of steam-cured precast concrete containing iron tailing powder. *Powder Technol.* **2019**, *345*, 292–299. [CrossRef]
3. Ince, C.; Derogar, S.; Gürkaya, K.; James Ball, R. Properties, durability and cost efficiency of cement and hydrated lime mortars reusing copper mine tailings of Lefke-Xeros in Cyprus. *Constr. Build. Mater.* **2021**, *268*, 121070. [CrossRef]
4. Oschatz, M.; Antonietti, M. A search for selectivity to enable CO_2 capture with porous adsorbents. *Energy Environ. Sci.* **2018**, *11*, 57–70. [CrossRef]

5. Plaza, M.G.; Gonazlez, A.S.; Rubiera, F.; Pevida, C. Water vapour adsorption by a coffee-based microporous carbon: Effect on CO$_2$ capture. *J. Chem. Technol. Biotechnol.* **2015**, *90*, 1592–1600. [CrossRef]
6. Meor Yusoff, M.S.; Muslimin, M.; Paulus, W. Effect of fractional precipitation on quality of nanostructured alumina produced from black aluminium dross waste. *Adv. Mater. Res.* **2011**, *173*, 24–28. [CrossRef]
7. Tsakiridis, P.E.; Oustadakis, P.; Agatzini-Leonardou, S. Aluminium recovery during black dross hydrothermal treatment. *J. Environ. Chem. Eng.* **2013**, *1*, 23–32. [CrossRef]
8. Lou, B.J.; Shen, H.L.; Liu, B.; Liu, J.; Zhang, S.G. Recycling secondary aluminum dross to make building materials: A review. *Constr. Build. Mater.* **2023**, *409*, 133989. [CrossRef]
9. Zhang, S.Y.; Wang, K.; Li, H.; Zhang, X.Q.; Jiang, Y.L. Novel SCMs produced by the calcination of secondary aluminium dross with dolomite and their potential usage in cemented paste backfill. *Constr. Build. Mater.* **2023**, *365*, 130119. [CrossRef]
10. Satish, R.; Neeraja, D. Mechanical and durability aspects of concrete incorporating secondary aluminium slag. *Resour. Effic. Technol.* **2016**, *2*, 225–232.
11. Yoshimura, H.N.; Abreu, A.P.; Molisani, A.L.; Camargo, A.C.; Portela, J.C.S.; Narita, N.E. Evaluation of aluminum dross waste as raw material for refractories. *Ceram. Int.* **2008**, *34*, 581–591. [CrossRef]
12. Zawrah, M.F.; Ghanaym, E.E.; Sadek, H.E.H.; El Defrawy, S.A.; Ali, O.A.M. Synthesis, characterization and sinterability of pure and Ni-doped nano layered double hydroxides from aluminum dross. *Ceram. Int.* **2019**, *45*, 17598–17610. [CrossRef]
13. Rotana, H.; Claudia, P.O. On utilization and mechanisms of waste aluminium in mitigating alkali-silica reaction (ASR) in concrete. *J. Clean. Prod.* **2019**, *212*, 864–879.
14. Socrates, P.M.P.; Juan, M.G.C. Influence of the secondary aluminum chip on the physical and mechanical properties of concrete. *Innov. Infrastruct. Solut.* **2023**, *8*, 45.
15. Kočí, V.; Vejmelková, E.; Koňáková, D.; Pommer, V.; Grzeszczyk, S.; Matuszek-Chmurowska, A.; Mordak, A.; Černý, R. Basic physical, mechanical, thermal and hygric properties of reactive powder concrete with basalt and polypropylene fibers after high-temperature exposure. *Constr. Build. Mater.* **2023**, *374*, 130922. [CrossRef]
16. Hong, X.; Wang, H.; Shi, F. Influence of NaCl freeze thaw cycles and cyclic loading on the mechanical performance and permeability of sulphoaluminate cement reactive powder concrete. *Coatings* **2020**, *10*, 1227. [CrossRef]
17. Suescum-Morales, D.; Silva, R.V.; Bravo, M.; Jiménez, J.R.; Fernández-Rodríguez, J.M.; Brito, J.D. Effect of incorporating municipal solid waste incinerated bottom ash in alkali-activated fly ash concrete subjected to accelerated CO$_2$ curing. *J. Clean. Prod.* **2022**, *370*, 133533. [CrossRef]
18. Kaliyavaradhan, S.K.; Li, L.F.; Ling, T.C. Response surface methodology for the optimization of CO$_2$ uptake using waste concrete powder. *Constr. Build. Mater.* **2022**, *340*, 127758. [CrossRef]
19. Boulahbal, A.I.; Santamaría, L.; Azizi, A.; Boutahala, M.; Korili, S.A.; Gil, A. Synthesis of Cu-Al layered double hydroxides from aluminum saline slags. *Miner. Eng.* **2023**, *204*, 108413. [CrossRef]
20. Bai, L.; Liu, H.; Wang, H. The Influence of CO$_2$-Cured Boiler Cinder on the Mechanical Strength of RPC Exposed to NaCl Erosion. *Coatings* **2023**, *13*, 1021. [CrossRef]
21. Alderete, N.M.; Joseph, A.M.; Van den Heede, P.; Matthys, S.; De Belie, N. Effective and sustainable use of municipal solid waste incineration bottom ash in concrete regarding strength and durability. *Resour. Conserv. Recycl.* **2021**, *167*, 105356. [CrossRef]
22. Jiang, H.; Wang, W.; Wang, H. The Corrosion Resistance of Reinforced Reactive Powder Concrete with Secondary Aluminum Ash Exposed to NaCl Action. *Materials* **2023**, *16*, 5615. [CrossRef] [PubMed]
23. Gursel, A.P.; Maryman, H.; Ostertag, C. A life-cycle approach to environmental, mechanical, and durability properties of "green" concrete mixes with rice husk ash. *J. Clean. Prod.* **2016**, *112*, 823–836. [CrossRef]
24. Tarangini, D.; Sravana, P.; Srinivasa Rao, P. Effect of nano silica on frost resistance of pervious concrete. *Mater. Today Proc.* **2022**, *51*, 2185–2189. [CrossRef]
25. Meshram, A.; Gautam, D.; Singh, K. Recycling of white aluminium dross: Production of potash alum. *Trans. Indian. Inst. Met.* **2020**, *73*, 1239–1248. [CrossRef]
26. Ismail, I.; Bernal, S.A.; Provis, J.L.; San Nicolas, R.; Brice, D.G.; Kilcullen, A.R.; Hamdan, S.; Deventer, J.S. Influence of fly ash on the water and chloride permeability of alkali-activated slag mortars and concretes. *Constr. Build. Mater.* **2013**, *48*, 1187–1201. [CrossRef]
27. Mahinroosta, M.; Allahverdi, A. A promising green process for synthesis of high purity activated-alumina nanopowder from secondary aluminum dross. *J. Clean. Prod.* **2018**, *179*, 93–102. [CrossRef]
28. Sarikaya, Y.; Sevinç, I.; Akinç, M. The effect of calcinations temperature on some of the adsorptive properties of fine alumina powders obtained by emulsion evaporation technique. *Powder Technol.* **2001**, *116*, 109–114. [CrossRef]
29. Serelis, E.; Vaitkevicius, V. Effect of waste glass powder and liquid glass on the Physico-Chemistry of Aluminum-Based Ultra-Lightweight concrete. *Constr. Build. Mater.* **2023**, *390*, 131615. [CrossRef]
30. Song, Y.; Li, B.; Yang, E.-H.; Liu, Y.; Ding, T. Feasibility Study on Utilization of Municipal Solid Waste Incineration Bottom Ash as Aerating Agent for the Production of Autoclaved Aerated concrete. *Cem. Concr. Compos.* **2015**, *56*, 51–58. [CrossRef]
31. Almeida, V.O.; Silvestro, L.; Gleize, P.J.; Kirchheim, A.P.; Schneider, I.A. Application of leached iron ore tailings to produce sustainable cements. *Constr. Build. Mater.* **2023**, *377*, 131095. [CrossRef]
32. Miguel, F.; Brito, J.D.; Silva, R.V. Durability-related performance of recycled aggregate concrete containing alkali-activated municipal solid waste incinerator bottom ash. *Const. Build. Mater.* **2023**, *397*, 132415. [CrossRef]

33. IV, G.M.; Sinnan, R.; Young, M. Evaluation of reclaimed municipal solid waste incinerator sands in concrete. *J. Clean. Prod.* **2019**, *229*, 838–849.

34. Feng, H.G.; Wang, L.; Li, G.; Jin, Q. Removal of impurities for the synthesis of high-property alumina-spinel ceramic from secondary aluminum dross. *Ceram. Int.* **2023**, *49*, 34616–34626. [CrossRef]

35. Xu, L.; Li, X.B.; Liu, Y.; Chen, M.; Wang, N. Recovery of low phosphorus iron from steel slag using secondary aluminum dross as the reductant. *J. Environ. Chem. Eng.* **2023**, *11*, 110973. [CrossRef]

36. Tran, H.; Sorelli, L.; Hisseine, O.A.; Bouchard, D.; Brail, V.; Sanchez, T.; Conciatori, D.; Ouellet-Plamondon, C. Development of sustainable ultra-high performance concrete recycling aluminum production waste. *Constr. Build. Mater.* **2023**, *371*, 130212. [CrossRef]

37. Aninda, S.S.; Islam, M.S. Effectiveness of waste concrete powder in fabricating compressed stabilized earth blocks: Strength, durability and thermal assessment. *J. Build. Eng.* **2023**, *80*, 107989. [CrossRef]

38. Liu, Q.; Zhang, Z.; Zhang, S.G.; Li, X.L.; Long, H.C.; Meng, X.X.; Melnikov, A.; Gagarin, L. The influence of particle morphology on the long-term strength of sandy soil under freeze-thaw cycles. *Case. Stud. Constr. Mater.* **2023**, *18*, e02196. [CrossRef]

39. Beltrame, N.A.M.; Dias, R.L.; Witzke, F.B.; Medeiros-Junior, R.A. Effect of carbonation curing on the physical, mechanical, and microstructural properties of metakaolin-based geopolymer concrete. *Constr. Build. Mater.* **2023**, *406*, 133403. [CrossRef]

40. Esmeryan, K.D.; Fedchenko, Y.I. Superhydrophobic soot as a mechanically robust, heat insulating and anti-corrosion protective coating for concrete surfaces. *Colloids Surf. A* **2023**, *672*, 131723. [CrossRef]